



Simplify your imaging workflows

**Make research imaging workflows accessible, traceable,
and secure with Athena Software for Core Imaging Facilities.**

Thermo Scientific™ Athena Software is a premium imaging data management platform designed for core imaging facilities that support materials science research.

Athena Software ensures traceability of images, metadata, and experimental workflows through an intuitive and collaborative web interface.

Find out more at thermofisher.com/athena

ThermoFisher
SCIENTIFIC

The Bottlenecks of Cs₂AgBiBr₆ Solar Cells: How Contacts and Slow Transients Limit the Performance

Maximilian T. Sirtl, Firouzeh Ebadi, Bas T. van Gorkom, Patrick Ganswindt, René A. J. Janssen, Thomas Bein,* and Wolfgang Tress*

Dedicated to Professor Karl Leo on the occasion of his 60th birthday

Cs₂AgBiBr₆ has attracted much interest as a potential lead-free alternative for perovskite solar cells. Although this material offers encouraging optoelectronic features, severe bottlenecks limit the performance of the resulting solar cells to a power conversion efficiency of below 3%. Here, the performance-limiting factors of this material are investigated in full solar cells featuring various architectures. It is found that the photovoltaic parameters of Cs₂AgBiBr₆-based solar cells strongly depend on the scan speed of the *J/V* measurements, suggesting a strong impact of ionic conductivity in the material. Moreover, a sign change of the photocurrent for bias voltages above 0.9 V during the measurement of the external quantum efficiency (EQE) is revealed, which can be explained by non-selective contacts. The radiative loss of the V_{OC} from sensitive subgap-EQE measurements is calculated and it is revealed that the loss is caused by a low external luminescence yield and therefore a high non-radiative recombination, supported by the first report of a strongly red shifted electroluminescence signal between 800 and 1000 nm. Altogether, these results point to a poor selectivity of the contacts and charge transport layers, caused by poor energy level alignment that can be overcome by optimizing the architecture of the solar cell.

1. Introduction

Due to their attractive optoelectronic properties and processing pathways, the interest in lead-based halide perovskites (APbX₃; A = methylammonium/formamidinium/Cs/Rb; X = Cl, Br, I) sky-rocketed during the last decade.^[1] The nature and energy of the widely tunable bandgap, a sufficiently high charge carrier mobility, and high defect tolerance as well as the simple low-temperature processing pathways make these materials promising candidates for applications such as X-ray detectors,^[2] light emitting diodes,^[3–5] and solar cells with power-conversion efficiencies having approached 25%.^[5–7]

Even though lead-based perovskites have outstanding potential for being implemented in solar cells, so far their large-scale application has been challenging due to the high toxicity of lead,^[8] as well as several issues regarding the low stability toward ambient conditions, UV-light, and humidity.^[1] While stability issues can be addressed to a large extent by intelligent device- or materials-design^[5,9–11] and proper


encapsulation,^[12] the toxicity issue can be addressed by substitution of the lead(II) ions with homovalent alternatives such as Sn²⁺ ions in a standard halide perovskite structure,^[13] the use of Bi³⁺ or Sb³⁺ as a substitute for Pb²⁺ ions to form Cs₃Bi₂X₉ (X = Cl/Br/I)^[13] or by a combination of a monovalent and a trivalent metal ion, resulting in one of the emerging double perovskites A₂M^IM^{III}X₆ (A = MA, Cs; M^I = Ag⁺, In⁺, Au⁺, Cu⁺; M^{III} = Bi³⁺, Sb³⁺; X = Cl, Br), that have been realized both in 3D, as well as in low-dimensional Ruddlesden–Popper structures.^[14–18]

Among the double perovskites investigated to date, Cs₂AgBiBr₆ appears to be one of the most promising candidates, featuring a long charge carrier lifetime of up to 550 ns in single crystals and above 200 ns in thin films,^[19,20] high stability and good solution processability, as well as a decent theoretically possible power conversion efficiency (PCE) for solar cells.^[19,21] Although first solar cell reports were published several years ago with an initial PCE of ≈2.5%,^[22] researchers so far have struggled to achieve a PCE exceeding 2.84% by using this material as absorber.^[20,23–30] Besides addressing the possibility to tune the rather large and indirect bandgap and more generally the absorption onset using additives and alloying,^[31–35] several studies have focused on the identification of the limiting

M. T. Sirtl, P. Ganswindt, Prof. T. Bein
Department of Chemistry and Center for NanoScience (CeNS)
University of Munich (LMU)
Butenandtstr. 11, 81377 Munich, Germany
E-mail: bein@lmu.de

Dr. F. Ebadi, Dr. W. Tress
Institute of Computational Physics (ICP)
ZHAW School of Engineering
Wildbachstr. 21, Winterthur 8400, Switzerland
E-mail: wolfgang.tress@zhaw.ch

B. T. van Gorkom, Prof. R. A. J. Janssen
Molecular Materials and Nanosystems & Institute for Complex
Molecular Systems
Eindhoven University of Technology
Eindhoven 5600 MB, Netherlands

 The ORCID identification number(s) for the author(s) of this article can be found under <https://doi.org/10.1002/adom.202100202>.

© 2021 The Authors. Advanced Optical Materials published by Wiley-VCH GmbH. This is an open access article under the terms of the Creative Commons Attribution-NonCommercial License, which permits use, distribution and reproduction in any medium, provided the original work is properly cited and is not used for commercial purposes.

DOI: 10.1002/adom.202100202

factors hampering the performance of this material in order to overcome these issues and to push the PCE of the solar cells toward the theoretical limit. Kentsch et al. revealed a large exciton binding energy in this material,^[36] and others showed that the material suffers from a rather large trap density, while a high annealing temperature of above 250 °C is necessary in order to form the perovskite film without any secondary phases in the film.^[22] Most recently, Longo et al. reported on limiting factors in complete solar cells, revealing that one factor hampering the solar cell efficiency is a small electron diffusion length while the hole-diffusion length is rather large.^[37] Much effort has been put into the optimization of crystallinity and orientation of thin films of Cs₂AgBiBr₆,^[20,38] as well as interface modifications,^[23,39,40] the improvement of the optoelectronic properties of single crystals^[41,42] or regarding the origin of the photoluminescence (PL).^[43,44] Yet, there is still no consensus on how to exactly interpret the absorption and emission features^[44,45] and how to explain the severe differences between reported optical data of nominally the same material. In particular, whether and how they affect solar-cell performance remains to be understood.

In this work, we analyze the limiting factors of full solar cell devices based on Cs₂AgBiBr₆, comparing devices with different architectures and comprising Cs₂AgBiBr₆ films obtained through different synthesis methods. We investigate the radiative voltage limit using sensitive external quantum efficiency (EQE) and photo- and electroluminescence (EL) measurements. We examine the internal photovoltaic (PV) quantum efficiency as a function of voltage and scan rate and reveal that photocurrent collection and charge carrier recombination strongly depend on the conditions set by the preceding voltage. Open circuit voltage transients provide further evidence regarding the interplay between properties of the contacts and possibly mobile ionic charges in the perovskite, thus modifying the selectivity of the contacts and interfacial recombination. We demonstrate that the latter process turns out to be a major loss mechanism.

2. Experimental Section

2.1. Materials and Thin Film synthesis

The stock solution was prepared by dissolving CsBr (212.8 mg, 1 mmol, 2 eq, Alpha Aesar, 99.999% metals basis), BiBr₃ (224.4 mg, 0.5 mmol, 1 eq, Alpha Aesar, 99.9% metals basis), and AgBr (93.9 mg, 0.5 mmol, 1 eq, Alpha Aesar, 99.998% metals basis) in 1 mL DMSO (Sigma Aldrich, anhydrous, ≥99.9%) at 130 °C to obtain a 0.5 M solution.

For preparing the solar cells on planar TiO₂ (see below for preparation), the thin films were deposited in a nitrogen filled glovebox by spin-coating dynamically (first at 1000 rpm for 10 s, followed by a second step at 5000 rpm for 30 s) onto the substrate (80 μL of the stock solution). After 23 s of the second step, 400 μL 2-propanol were dripped quickly on top of the substrate and the films were annealed afterward at 275 °C for 5 min.

For thin films on mesoporous (mp)-TiO₂, the substrates and the precursor solution were pre-heated at 85 °C on a Heidolph-hotplate with an internal temperature sensor. 100 μL of the heated precursor-solution were spincoated dynamically (2000 rpm, 45 s) hot onto the heated substrates at ambient conditions in air.

2.2. Solar Cell Fabrication

Fluorine-doped tin oxide coated glass sheets (7 Ω sq⁻¹) were patterned by etching with zinc-powder and 3 M HCl, cleaned with a detergent followed by washing with acetone and ethanol and dried under an air stream. Directly before applying the hole-blocking layer, the substrates were oxygen plasma cleaned for 5 min.

2.3. c-TiO₂

A compact (c)-TiO₂ layer was prepared from a sol-gel precursor solution by spin-coating 100 μL onto the 3 cm × 3 cm substrates for 45 s at 2000 rpm and calcination afterward at 500 °C for 30 min in air, resulting in a 50 nm thick layer. For the sol-gel solution, 2 M HCl (35 μL) in 2.53 mL dry 2-propanol was added dropwise to a solution of 370 μL of titanium isopropoxide in 2.53 mL dry 2-propanol under vigorous stirring. After cooling down, the substrates were again plasma cleaned for 5 min and transferred to a nitrogen-filled glovebox. On top of the compact titania layer, the active layer was deposited as described above.

2.4. mp-TiO₂

After the deposition of the layer of c-TiO₂, 100 μL of a dispersion of mp-TiO₂ nanoparticles (DyeSol, 3:1 EtOH:TiO₂-paste) was spincoated on top of the c-TiO₂ layer without plasma-cleaning. Afterward, the substrates were calcined at 500 °C for 30 min at air resulting in a 500 nm thick layer. After cooling down, the active layer was deposited on top of the TiO₂ layer as described above.

2.5. Deposition of HTM

For poly(3-hexylthiophen-2,5-diyl) (P3HT), 55 mg of the material (Ossila, batch M1011; MW: 60150; RR: 97.6%, Mn: 28650 PDI: 2.1) was dissolved in 1 mL ortho-dichlorobenzene and deposited by spin-coating 75 μL of a 55 mg mL⁻¹ solution statically at 600 rpm for 120 s at ambient conditions in air. The gold electrode (see below) was deposited directly after the HTM deposition.

For 2,2',7,7'-tetrakis-(N,N-di-4-methoxyphenylamino)-9,9'-spirobifluorene (Spiro-OMeTAD, Borun Chemicals, 99.5% purity), 73 mg of the material was dissolved in 1 mL of chlorobenzene. To this solution, 10 μL of 4-*tert*-butylpyridine and 30 μL of a bis(trifluoromethane)sulfonamide lithium salt solution (170 mg in 1 mL acetonitrile) were added. The resulting HTM solution was deposited via dynamic spincoating (1500 rpm, 45 s) in a nitrogen-filled glovebox. Afterward, the samples were stored overnight in air at < 30 R.H. to allow the HTM to oxidize.

The top electrode with a thickness of 40 nm was deposited by thermally evaporating gold under vacuum (at ≈10⁻⁷ mbar).

2.6. Materials Characterization

The thin film XRD data were recorded using a Bruker D8 Discover Diffractometer with Ni-filtered Cu Kα radiation

and a LynxEye position-sensitive detector in Bragg-Brentano Geometry.

2.7. SEM

SEM images were obtained with an FEI Helios G3 UC instrument with an acceleration voltage of 5 kV for the cross-sectional images and 2 kV for the top-view images. All samples were sputtered with carbon beforehand and both mirror and through-lens detectors were used.

2.8. Steady State PL

The thin films were deposited onto the respective substrate by spin-coating as described above and all PL measurements were performed with a FluoroTime 300 Spectrofluorometer (PicoQuant GmbH) in air.

To excite the samples for steady state measurements, a pulsed solid-state laser (wavelength 375 nm; LDH375, PicoQuant) with a fluence of 20 pJ cm^{-2} at 40 MHz repetition rate was used in order to simulate steady state conditions.

2.9. Solar Cell Characterization

Current–voltage (J/V) characteristics of the perovskite solar cells were measured using a Newport OrielSol 2A solar simulator with a Keithley 2401 source meter. The devices were illuminated through a shadow mask, yielding an active area of 0.0831 cm^2 . The J/V curves were recorded under standard AM 1.5G illumination with a xenon lamp, and calibrated to a light intensity of 100 mW cm^{-2} with a Fraunhofer ISE certified silicon diode. The input bias voltage was scanned from -1.5 to 0 V in 0.01 V steps with a rate of 0.1 V s^{-1} for the standard PCE measurements. For the experiments with different scan-speeds, we chose bigger voltage steps varying from 0.01 V to 1 V . All prepared devices show a comparable degree of hysteresis between the forward and the reverse scan.

2.10. Film Thickness Determination

The film thickness was determined using SEM cross-sectional images shown in the SI.

2.11. Sensitive EQE Measurements

Sensitive EQE measurements to characterize the sub-bandgap region were conducted using a halogen lamp (Osram 64655 HLX 250 W) as illumination source. The light was chopped using an Oriel 3502 chopper at 330 Hz and subsequently passed through a double-grating monochromator (Oriel, Cornerstone 260). Several long-pass filters were used to filter out stray light. The samples were mounted in an air tight holder filled with nitrogen to prevent air exposure. The response was recorded with a pre-amplifier (Stanford Research, SR 570) using a lock-in

amplifier (Stanford Research, SR 830) and calibrated using two Si and InGaAs reference cells.

2.12. EQE and Transmission Measurements for Figure 3

Measurements were performed on a homemade system with a halogen lamp, a monochromator and a silicon reference diode. The light was chopped at 330 Hz and the signal was detected through a lock-in amplifier. The setup was calibrated with a silicon solar cell, which was also used for transmission measurements, where it was placed behind the sample. Bias light was provided by blue LEDs.

2.13. J/V Loops and EL

Voltage was applied and current measured with a potentiostat (Biologic SP300). Illumination was provided by a blue LED. For the ELQE, the current of a 1 cm^2 silicon diode (Hamamatsu) placed in close vicinity to the sample was measured by a second channel of the potentiostat. For the EL spectrum, a constant current of 10 mA was applied and the spectrum was measured with a CCD Spectrometer (Andor with iDUS detector).

2.14. Transient Photovoltage

This measurement was performed with a Paios instrument (Fluxim) and a blue LED.

3. Results and Discussion

Our recent work has established the successful synthesis of thin film solar cells based on $\text{Cs}_2\text{AgBiBr}_6$ using both the antisolvent method under inert conditions^[20] and the one-step spincoating method under ambient conditions without an antisolvent.^[22] After deposition of the thin films using both techniques, we obtained phase pure, yellow films that were opaque by using no antisolvent at ambient conditions (inset **Figure 1a**) and transparent by using 2-propanol as an antisolvent inside the glovebox (inset **Figure 1a**). The different spincoating techniques result in a large difference in the film thickness, which was determined to be $\approx 130 \pm 12 \text{ nm}$ for the antisolvent method and $550 \pm 35 \text{ nm}$ when using no antisolvent. The layer thicknesses were determined using the scanning electron microscopic (SEM) images in **Figure S1**, Supporting Information. The Bragg–Brentano X-ray diffraction (XRD) patterns in **Figure 1a** confirm the phase-pure formation of the desired $\text{Cs}_2\text{AgBiBr}_6$ thin films after annealing at $275 \text{ }^\circ\text{C}$ for 5 min and at $285 \text{ }^\circ\text{C}$ for 5 min, respectively.

The XRD patterns show differences in the number and intensity of the peaks, which match all with the theoretical pattern obtained from single crystal data. The difference between the patterns could be explained by the large difference in the thickness of the thin films, which is more than three times greater for the films fabricated without using an antisolvent. The PL spectra in **Figure 1c** show for both films the characteristic broad peak with a maximum at ≈ 605 and 615 nm , which is

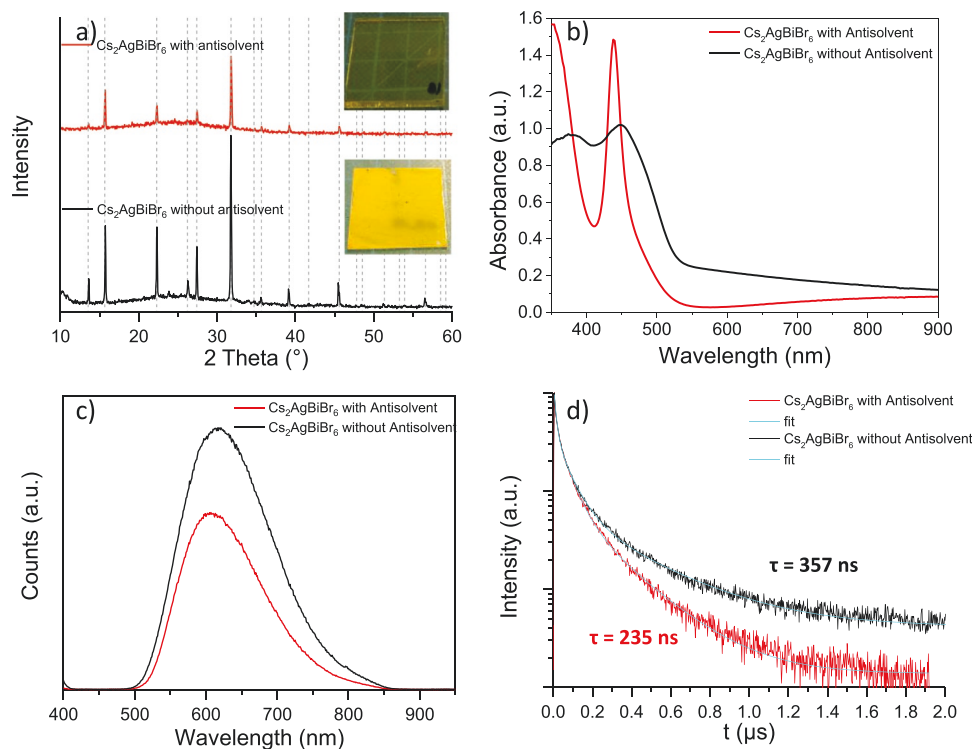


Figure 1. XRD patterns, PL spectra, and UV/Vis spectra of the differently spincoated $\text{Cs}_2\text{AgBiBr}_6$ thin films. a) XRD patterns measured in Bragg–Brentano geometry of the thin films spincoated without (black line) and with antisolvent (red line), with an image of the resulting films in the respective inset. The peaks of the theoretical pattern are indicated by grey, dashed droplines. b) The respective UV/Vis spectra of the thin films spincoated with (red line) and without antisolvent (black line). c) plots of the steady state PL measurements for the thin films spincoated with (red line) and without antisolvent (black line). d) Results of the TCSPC measurements with the films spincoated with (red line) and without (black line) antisolvent. Triple-exponential fits are shown in turquoise, giving the longest-living fraction of 235 ns with the antisolvent and of 357 ns without the antisolvent.

in agreement with literature reports.^[22,27,28,30] The rather small difference in the peak intensity between the two synthesis methods indicates a luminescence yield of the same order of magnitude for the films resulting from the different methods. A change can also be seen in the photoluminescence (PL) lifetimes of the different films (Figure 1c). While both values are in the range reported in the literature, films spincoated using the antisolvent method show a charge carrier lifetime of 235 ns (red line) while the films spincoated without antisolvent show an increase of the lifetime to 357 ns (black line). Although this trend confirms the trend in the PL intensity, it is a minor effect, which hardly influences the solar cell performance.

The biggest difference between thin films resulting from the different synthesis methods can be found in the UV/Vis spectra in Figure 1b) obtained from transmission measurements. Whereas the absorption onset at ≈ 550 nm (2.3 eV) remains unmodified, the absorbance in this spectral range (450 to 550 nm) is increased for the film without antisolvent (in contrast to the sharp peaks discussed below). This trend is consistent with an increased thickness of the film without antisolvent, although not quantitatively matching the changes of the thickness by a factor of four, which might be explained by the mesoporous TiO_2 (mp- TiO_2) present in the film and a non-compact film. The underlying transition at the absorption onset is known from calculations to be an X to L point transition,^[46] confirming the experimental reports on the indirect bandgap.^[14,19] Strikingly, the absorption features peaking at 340 nm (3.6 eV) and 440 nm (2.8 eV), are less pronounced

and even lower for the much thicker film. Commonly, they are attributed to direct transitions,^[46] where there seems some dispute whether the narrow peak at 440 nm is due to a strongly bound exciton (direct bandgap at 387 nm (3.2 eV))^[36,45] or not.^[44] In our case, the decrease of the two peaks is correlated, which would be consistent with the same direct nature of the transitions (free, exciton). Nevertheless, the question remains why this transition is so strong in the thinner film and why it does not scale with the film thickness as the indirect transition at the absorption onset at 550 nm does. We speculate whether this observation could be due to a morphology effect related to a preferred orientation of the thinner film or a high presence of scattering nanocrystals.^[47] An alternative explanation would be that different amounts of impurity phases (undetected by diffraction) are present in the two films. Possible crystalline secondary phases can, however, be excluded by the experimental XRD pattern. Moreover, the used deposition techniques are well known to produce $\text{Cs}_2\text{AgBiBr}_6$ -thin films without detectable impurity phases.

The direct impact on the performance of solar cells based on the different films will be discussed further in the remainder of the paper.

3.1. Solar Cells

To better understand the performance limiting factors of $\text{Cs}_2\text{AgBiBr}_6$ solar cells, we fabricated devices using the

Table 1. Solar cell parameters of all solar cells investigated in this study using different ETL/HTM combinations. The first value shows the respective value of the champion cell while the averages with standard deviation are shown in parentheses.

Number of cells	J_{SC} [mA cm^{-2}] (Avg)	V_{OC} [V] (Avg)	FF [%] (Avg)	PCE [%] (Avg)
FTO/c-TiO ₂ /Cs ₂ AgBiBr ₆ /P3HT/Au				
170	1.35 (1.26 ± 0.13)	1.08 (0.98 ± 0.05)	71 (63 ± 5)	1.04 (0.78 ± 0.13)
FTO/c-TiO ₂ /Cs ₂ AgBiBr ₆ /Spiro-OMeTAD/Au				
44	1.38 (1.10 ± 0.10)	0.87 (0.74 ± 0.11)	57 (57 ± 8)	0.70 (0.46 ± 0.09)
FTO/c-TiO ₂ /mp-TiO ₂ /Cs ₂ AgBiBr ₆ /P3HT/Au				
27	2.35 (2.10 ± 0.31)	0.85 (0.90 ± 0.07)	55 (51 ± 6)	1.10 (0.95 ± 0.10)
FTO/c-TiO ₂ /mp-TiO ₂ /Cs ₂ AgBiBr ₆ /Spiro-OMeTAD/Au				
20	2.50 (2.38 ± 0.13)	1.02 (0.93 ± 0.09)	55 (54 ± 6)	1.40 (1.20 ± 0.12)

architecture FTO/ETL/Cs₂AgBiBr₆/HTM/Au with either compact TiO₂ (c-TiO₂) or a combination of c-TiO₂ and mesoporous (mp) TiO₂ as electron transport layer (ETL), as well as with either 2,2',7,7'-tetrakis[N,N-di(4-methoxyphenyl)amino]-9,9'-spirobifluorene (Spiro-OMeTAD) or poly(3-hexylthiophene) (P3HT) as hole transporting material (HTM). The solar cells that use mp-TiO₂ were fabricated without using an antisolvent, while cells comprising solely c-TiO₂ were prepared using an antisolvent-process. The active area was ≈0.16 cm² and reduced to 0.083 cm² by an aperture for the measurements under the solar simulator.

The main focus of this study was on a detailed investigation of solar cells with c-TiO₂ as ETL and P3HT as HTM, hence the number of solar cells using these materials exceeds the number of cells with other HTM/ETL combinations. **Table 1** shows the parameters of the solar cells investigated in this study. The box plots of the J_{SC} , V_{OC} , FF , and PCE data of all solar cells measured in this work can be found in Figure S2, Supporting Information.

The results show values for the PCE that are statistically reliable for further investigation of the optoelectronic properties of the films, as well as for the determination of the performance limiting factors with PCE values between 0.7 and 1.4%.

Cells comprising Spiro-OMeTAD on c-TiO₂ show the lowest efficiency of all cells with 0.7% PCE for the champion cell and 0.46% on average for more than 40 solar cells. This is related to a rather small V_{OC} and FF of only 0.87 (0.74) V and 57%, respectively. Cells comprising P3HT as HTM on c-TiO₂ show a remarkably higher PCE with values above 1% and an increase in both FF and J_{SC} by 10% and 25% on average. Both architectures, however, suffer from a very low J_{SC} .

The biggest difference between all cells can be found in the J_{SC} of the mp-TiO₂ and c-TiO₂ cells, which agrees with early reports on Cs₂AgBiBr₆ solar cells^[22] and indicates enhanced charge collection by the mesoporous structure. Moreover, using the one-step spincoating technique allows one to produce thicker films compared to the antisolvent method, however solar cells produced with this method suffer from a rather rough film morphology. Therefore, to access the benefits of a thicker layer with this technique, a mesoporous scaffold is necessary for an effective charge extraction.

The results show that a further optimization of the mp-cells is necessary as the devices fabricated on the mp scaffold suffer from a rather low FF . Still, the increased J_{SC} results in a higher

PCE for all cells on mp-TiO₂ compared to planar devices. The comparison of the Spiro-OMeTAD cells shows an increase in the PCE by 100% for the champion cell and even higher in average, which is also caused by an increase in the V_{OC} . The P3HT devices do not show such a large improvement in the PCE, which can be related to a rather low V_{OC} in addition to the low FF . The results show the potential of mp-TiO₂ to help to optimize charge extraction from the Cs₂AgBiBr₆ double perovskites.

From all measured solar cells, we selected a smaller group that show a representative performance to investigate the impact of a fast J/V -scan on the chosen cells as discussed in the following.

3.2. Scan-Rate Dependent J/V Curves

The scan speed used to identify the J/V characteristics of solar cells reportedly shows a large influence for devices based on ionic materials such as perovskites.^[48–50] This circumstance led to a standardization of the measurement protocol for lead-based perovskites and the necessity for reporting this protocol in publications.^[51] However, this is not yet the case for reports on the efficiency of Cs₂AgBiBr₆ based solar cells, where scan speeds are commonly not reported, although hysteresis is mentioned in some publications^[28,40] and the material is assumed to show ionic conductivity.^[24]

To further investigate the effect of the ionic character of the material on the solar-cell performance, we performed J/V -scans at different scan speeds, varying from 0.01 V-steps up to 1 V-steps under 1 sun illumination for several of the solar cells discussed above. The results in **Table 2** and **Figure 2** show that changing the scan-speed strongly influences the photocurrent obtained from the solar cells for all architectures.

The biggest effect can be seen with cells comprising Spiro-OMeTAD as an HTM, where the J_{SC} increased from 1.2 mA cm⁻² for 0.01 V/step to 2.6 mA cm⁻² for 1 V/step for the cells on c-TiO₂, while the change on mp-TiO₂ is similar with an increase of 1.8 to 3.7 mA cm⁻² which corresponds to a relative increase of 116% and 105%, respectively. When using P3HT as an HTM, a similar effect was observed which, however, is not as big as for Spiro-OMeTAD with an increase of the J_{SC} from 1.2 to 2 mA cm⁻² ($\Delta J_{SC} = 67\%$) for c-TiO₂ and 1.7 to 2.4 mA cm⁻² ($\Delta J_{SC} = 41\%$) for mp-TiO₂. In Figure 2 a,b,d,e, we show the J/V

Table 2. Overview of the solar cells of various architectures measured with different scan speeds. The table shows the different J_{SC} values for varying scan speeds (0.01 V/step–1 V/step where one step takes one second) together with the relative J_{SC} -change in percent. Underneath we show the resulting PCE of the corresponding cell and scan. We note that the V_{OC} and FF values for scans faster than 0.1 V/step were not reliable for calculating the PCE. The Hysteresis Index was calculated as $(PCE(reverse) - PCE(forward)) / PCE(reverse)$. The captions in the grey bars indicate the different architectures used for the solar cells.

Scan-Speed	0.01 V/step	0.05 V/step	0.1 V/step	0.5 V/step	1 V/step
FTO/c-TiO ₂ /Cs ₂ AgBiBr ₆ /Spiro-OMeTAD/Au					
J_{SC}	1.2 mA cm ⁻²	1.4 mA cm ⁻²	1.6 mA cm ⁻²	2.5 mA cm ⁻²	2.6 mA cm ⁻²
Increase		16%	33%	108%	116%
PCE	0.56%	0.62%	0.66%		
Hysteresis index	0.16	0.27	0.33		
FTO/c-TiO ₂ /mp-TiO ₂ /Cs ₂ AgBiBr ₆ /Spiro-OMeTAD/Au					
J_{SC}	1.8 mA cm ⁻²	2.3 mA cm ⁻²	2.8 mA cm ⁻²	3.6 mA cm ⁻²	3.7 mA cm ⁻²
Increase		27%	56%	100%	105%
PCE	1.23%	1.29%	1.33%		
Hysteresis index	0.27	0.36	0.35		
FTO/c-TiO ₂ /Cs ₂ AgBiBr ₆ /P3HT/Au					
J_{SC}	1.2 mA cm ⁻²	1.4 mA cm ⁻²	1.5 mA cm ⁻²	1.9 mA cm ⁻²	2.0 mA cm ⁻²
Increase		16%	25%	58%	67%
PCE	0.82%	0.88%	0.92%		
Hysteresis index	0.10	0.27	0.39		
FTO/c-TiO ₂ /mp-TiO ₂ /Cs ₂ AgBiBr ₆ /P3HT/Au					
J_{SC}	1.7 mA cm ⁻²	1.9 mA cm ⁻²	2.1 mA cm ⁻²	2.3 mA cm ⁻²	2.4 mA cm ⁻²
Increase		12%	24%	35%	41%
PCE	0.97%	1.02%	1.04%		
Hysteresis index	0.03	0.13	0.18		

curves obtained with the measurements of up to 0.1 V/step. As expected, the PCE values of the investigated cells increase with the resulting J_{SC} by factors of 11 to 15% for planar devices and between 7 and 8% for the mp devices. We note that the curves show no change for the V_{OC} and the FF . We further observed a change in the hysteresis of the investigated cells. Figure 2d) shows another remarkable effect of faster scanning: For the 0.01 V/step, the J/V -curve expresses a large bump, which is caused by a J_{SC} smaller than the J -values at $V > 0$ V and may be attributed to ionic drifts within the solar cell happening on a similar time scale as the J/V scan. The changing density of accumulated ionic charges during the J/V scan results in a modified charge-carrier collection efficiency, which is reduced for lower voltages, where ions screen the built-in potential. As this trend of reduced charge collection efficiency at J_{SC} is against the electronic J/V curve, where charge collection efficiency increases from open circuit to short circuit, such a bump can occur.^[52,53] This bump, however, vanished for faster scan speeds, which further emphasizes the scan-speed dependence of the performance of the solar cells.

While the cells measured at slow scan speeds show only very low or negligible hysteresis, this effect increases with faster scan-speed, an effect observed for all investigated cells. Interestingly, the hysteresis is smaller for P3HT as HTM and mp-TiO₂ as ETL. Especially solar cells with mp-TiO₂ and P3HT show almost no hysteresis (HI = 0.03) while cells comprising Spiro-OMeTAD in both architectures show a rather large hysteresis

compared to cells with P3HT as HTM, further emphasizing the strong influence of the HTM on the effect of the ionic behavior of the solar cells.

As the results show a big impact of the J/V -scan speed on the solar cell performance, it is necessary to consistently report the exact measurement settings of the reported solar cells and, if possible, provide MPP tracked data.

3.3. Internal PV Quantum Efficiency and Transient Phenomena

While the J/V scan speed used to characterize the solar cells can have a large impact on the resulting performance parameters and increases the J_{SC} , the experimentally achieved current is still lower than what would be expected from optical absorption. To gain further insights, we investigated the external quantum efficiency (EQE) spectra of the solar cells and calculated the internal quantum efficiency (IQE) to discriminate between absorption and charge-carrier collection losses. The black line in Figure 3a) shows the EQE, measured at short circuit for a planar device. The EQE of the planar device roughly follows the absorption features in Figure 1d and mirrors the transmission spectrum of a perovskite film on glass/FTO, shown in blue. The EQE of the planar device cannot be enhanced with bias light and yields a current of 1.26 mA cm⁻² under AM1.5G, which is in good agreement with the solar simulator data. Contrary to that, the EQE spectra for a mesoporous

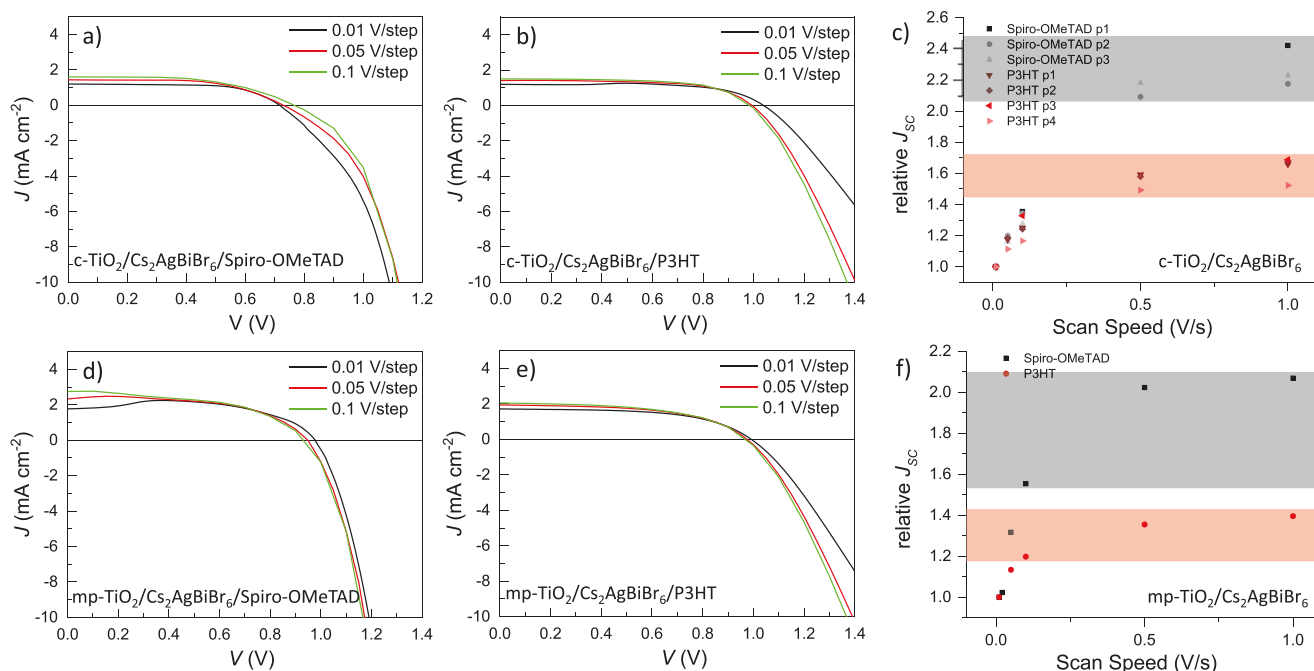


Figure 2. J/V -curves of different solar cell architectures measured with different scan-speeds. a) FTO/ $c\text{-TiO}_2/\text{Cs}_2\text{AgBiBr}_6/\text{Spiro-OMeTAD}/\text{Au}$, b) FTO/ $c\text{-TiO}_2/\text{Cs}_2\text{AgBiBr}_6/\text{P3HT}/\text{Au}$, d) FTO/ $c\text{-TiO}_2/\text{mp-TiO}_2/\text{Cs}_2\text{AgBiBr}_6/\text{Spiro-OMeTAD}/\text{Au}$, e) FTO/ $c\text{-TiO}_2/\text{mp-TiO}_2/\text{Cs}_2\text{AgBiBr}_6/\text{Spiro-OMeTAD}/\text{Au}$. All J/V -curves have the same color-coding with black for 0.01 V/step, red for 0.05 V/step and green for 0.1 V/step. c) Relative J_{sc} -values of several different solar cells with the architecture FTO/ $c\text{-TiO}_2/\text{Cs}_2\text{AgBiBr}_6/\text{HTM}/\text{Au}$ with Spiro-OMeTAD (black) and P3HT (red) as HTMs. f) Relative J_{sc} -values of one solar cell each with the architecture FTO/ $c\text{-TiO}_2/\text{mp-TiO}_2/\text{Cs}_2\text{AgBiBr}_6/\text{HTM}/\text{Au}$ with Spiro-OMeTAD (black) and P3HT (red) as HTMs. Panels (c) and (f) are provided with a guidance for the eye for the value-increase of the highest J_{sc} -changes, with black for Spiro-OMeTAD as HTM and red for P3HT as HTM.

device, shown in Figure 3b, demonstrate that blue bias light enhances the EQE. However, this behavior is well known for dye-sensitized solar cells on mp-TiO_2 and attributed to reduced surface recombination of mp-TiO_2 for higher photogenerated charge carrier densities.^[54]

In a next step, the EQE spectra were measured as a function of the applied voltage for the planar device (Figure 3c). The EQEs hardly change for voltages up to 0.8 V, which is consistent with a decently high FF of these devices (>70%, Table 1). However, independent of bias light and the actual V_{oc} obtainable under the illumination by the EQE measurement (0.35 V without, and 0.86 V with bias), the signal changes rapidly at 0.9 V (Figure S3, Supporting Information). As indicated by the massive drop in the EQE for the 0.9 V bias, the EQE signal changes sign and the (absolute) EQE increases with higher voltages. The strong drop of the EQE at 0.9 V is an indication for a built-in potential of ≈ 0.9 V. The change of sign of the EQE and photocurrent (difference between current under illumination and in the dark) is not uncommon for emerging PV and can be explained either by a photoconductivity effect, which enhances the forward injection current, or by the current of the photogenerated charge carriers themselves changing sign. Due to the high IQEs under forward bias, we think the former is more likely.^[55]

Interestingly, not only absolute values, but the spectral shapes of the EQE change, yielding for higher voltages a more pronounced EQE in spectral regions where the EQE spectra recorded at voltages below 0.9 V have a smaller signal. To better assess this effect, we approximate the IQE (or charge carrier

collection efficiency) by dividing the EQE by the absorption spectrum deduced from the measured and normalized transmission data of the film (from Figure 3a). Please note that for a more accurate description optical modeling would be required. However, as the subsequent layers (P3HT, Au) are hardly reflective but absorptive in the spectral range under investigation, reflection and interference effects are negligible. The IQEs obtained in this way, plotted in Figure 3d, are reliable and reveal a strong dependence on the wavelength. For voltages < 0.9 V, the IQE is highest in the absorption maxima, as also observed in ref. [37] where it is attributed to a low electron diffusion length reducing the collection probability of charges generated further away from the TiO_2 . As the IQE of the two peaks at 360 and 435 nm is comparable and assuming that the absorption at 435 nm is excitonic,^[36] we do not see a lower probability for harvesting photocurrent from excitonic excitations.

We do not wish to claim that we can extract a value for the diffusion length from these device measurements. The diffusion length is a parameter of a material or film, which has been reported to be larger than 100 nm for electrons and holes^[56] and high EQEs have been achieved with $\text{Cs}_2\text{AgBiBr}_6$.^[23] Instead, the IQE trend can as well be explained by space charge layers and field distributions arising in the solar cell due to a built-in potential, doping, and recombination processes at interfaces. Furthermore, an almost complete quenching of the $\text{Cs}_2\text{AgBiBr}_6$ PL in the device indicates that neither excitons nor immobile charges (i.e., those that do not contribute to J_{sc}) remain in the film but reach the “wrong” contacts and recombine instead (Figure S4, Supporting Information). Especially on the HTL

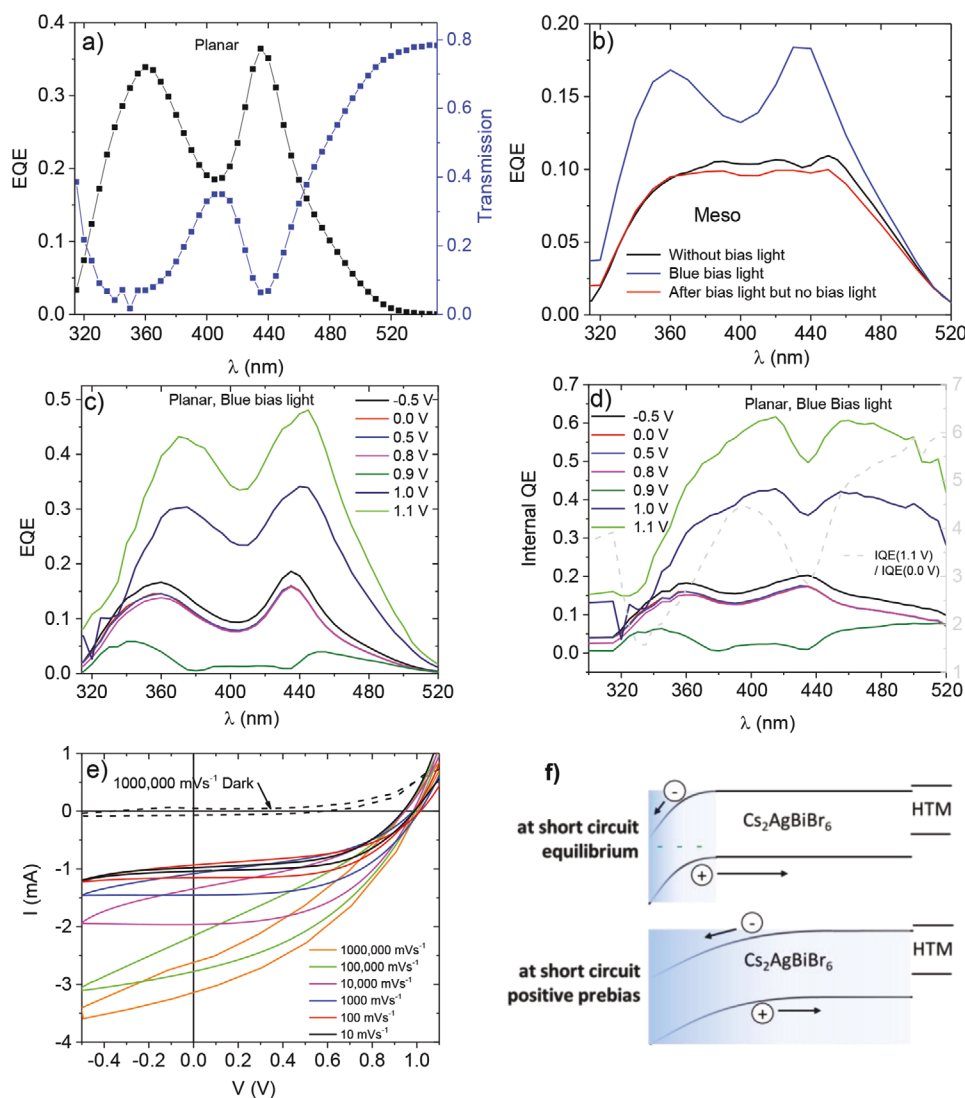


Figure 3. The current-collection bottleneck. a) EQE (black line) of planar device, plotted together with the transmission spectrum (blue line) of glass/FTO/Cs₂AgBiBr₆. b) EQE of mesoporous device with and without bias light, c) EQE of planar device for various applied voltages. For voltages larger than 0.9 V, the photocurrent changes sign. d) IQE derived from data in (c). The dashed line (right axis) shows the IQE at 1.1 V relative to those below 0.9 V. e) J/V loops at different scan rates and after prebias at 1.1 V. The dark curve at 1000 V s⁻¹ shows that capacitive effects are still negligible. f) Sketch of proposed band diagrams, indicating that mainly a narrow region close to the ETL commonly contributes to photocurrent (shaded). This region gets extended after a positive prebias, possibly because negative ionic charges close to the ETL were removed.

side, it is very likely that there is no energy barrier for electrons that could make this contact selective, which applies in particular for the P3HT device as the HOMO-LUMO difference of P3HT is even smaller than the bandgap of the double perovskite (Figure S5, Supporting Information). Here, a heterojunction of type 1 is probably formed, which would directly explain why excitons generated in P3HT (clearly seen in the absorption in Figure S6, Supporting Information) are not split at this junction and thus do not contribute to the photocurrent (no signal in the EQE).

For voltages ≥ 0.9 V, previous maxima become minima (pronounced at 435 nm). The relative normalized change ($\text{IQE}(1.1 \text{ V}) / \text{IQE}(0.0 \text{ V})$), plotted as a dashed line, clearly shows that this “inversion” holds for both absorption maxima. This means that the part of the perovskite layer closer to the HTL

is less conductive in the dark than the part close to the TiO₂. It might be possible that the forward current is driven mainly by electrons, as the hole injection barrier at the HTL is too high. The electrons would have to pass through the whole device and recombine with holes located on the HTL at the HTL interface. This electron current might profit from a conductivity enhancement within the whole layer and would be consistent with a non-selective interface at the HTL.

As already discussed above, the J/V curves show a rate-dependent hysteresis. Thus, we investigated the relation between hysteresis and the rather low observed EQE in more detail. We kept the solar cell under forward bias (1.1 V) for 10 s and performed a J/V -loop with varied sweep rate. The resulting J/V curves of the same device used for the EQE measurements are displayed in Figure 3e. The curves show that the

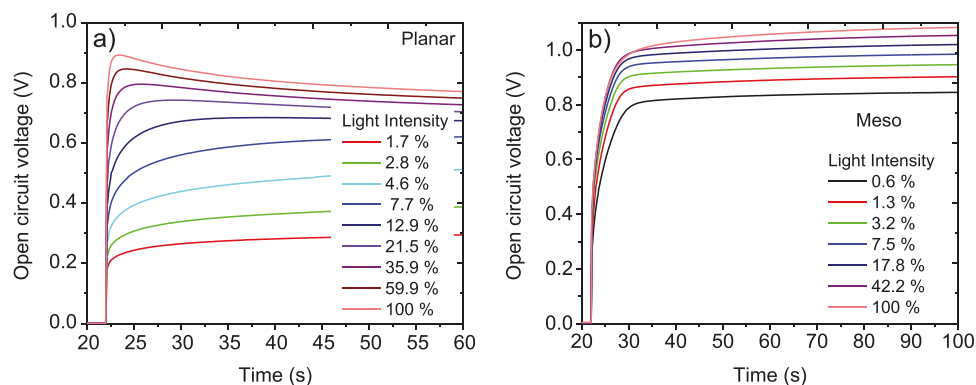


Figure 4. Transients of open circuit voltage. a) Planar device, b) mesoporous device. Light of different intensity is turned on at 22 s and light intensity is color-coded as indicated in the legend and is given in percent of 3 suns.

photocurrent is higher the faster the measurement is done after the prebias. Thus, the EQE can be boosted by a factor of 3 if the electric field distribution in the device is beneficial for charge extraction. In analogy to discussions on hysteresis in the lead-based perovskites, this can be explained by mobile ionic charges that, remaining at their position set by the forward bias, are not capable of screening the field induced by the fast backward scan.^[52] Interestingly, the behavior is very similar to observations in our previous work on lead-based perovskites on planar TiO₂,^[57] leading us to conclude that a proper choice of charge transport layers and interface properties will allow for high IQE in the double perovskite solar cells as well.

This conclusion also holds for the open-circuit voltage, which is strongly influenced by slow transient processes as shown in **Figure 4**, where measurements on a planar device compared to a mesoporous device are shown. For both architectures, reversible transients on the timescale of seconds are observed, which indicate that recombination probabilities, most likely at interfaces, change slowly. An explanation for the (initial) increase of V_{OC} could be that the photo-induced voltage leads to a redistribution of mobile ions in the perovskite that leads to a more selective solar cell by modifying the effective built-in potential. Shifted ions would screen the electric field less and would alleviate losses by shunts, which are dominating the strong dependence of V_{OC} on light intensity at low light intensities for the planar device. In the longer run, the maximum V_{OC} for high light intensities cannot be maintained, in particular for the planar device, whereas mp-TiO₂ shows a stabilization effect, possibly better maintaining a certain selectivity thus further indicating the strong impact of the charge extraction layer.

3.4. Emission, Absorption, and the Open-Circuit Voltage

We have already mentioned that the contacts are most likely a major source of recombination losses and therefore a low V_{OC} . In the following, we discuss V_{OC} in the context of absorption and emission features. The V_{OC} of the fabricated solar cells is ≈ 1.0 V, which is a rather low value for a material that absorbs at energies > 2.3 eV and shows a PL peaking between 610 and 630 nm (≈ 2 eV). Therefore, we expect high non-radiative recombination losses, as already stated in ref. [37]. However, the PL peak is rather broad and various values have been reported

for the bandgap of Cs₂AgBiBr₆.^[14,19,22,27,40] Therefore, a more detailed analysis is required.

First, we determine the radiative limit of the V_{OC} , that is, the theoretical maximum, following the opto-electronic reciprocity relation introduced by Rau.^[58] This approach was successfully applied to lead-based perovskite solar cells.^[59] The black solid line in **Figure 5a** shows the EQE obtained from a sensitive measurement and plotted versus energy for a device with Spiro-OMeTAD as HTL (for more devices see Figure S7, Supporting Information). The peak at 2.8 eV (yellow region) corresponds to the peak in Figures 3 and 1d at 445 nm, which is commonly attributed to the direct bandgap. Below this peak, there is another broad feature, which gives rise to a shoulder at ≈ 2.5 eV and a tail observable down to 2.1 eV (grey region). At energies below 2.1 eV there are further tail features (blue region), which we ignore for the moment. The broad onset between 2.1 and 2.6 eV (grey region) is also seen in absorption data from photo-thermal deflection spectroscopy, where an Urbach energy of 70 meV has been reported.^[37] If our EQE onset is fitted with an exponential function, a characteristic (“Urbach”) energy of 40 to 50 meV is determined, dependent on the selected energy range. However, an exponential function is not ideal for fitting this spectral range (grey) as we discuss in the following.

To better understand the EQE onset, we plot the slope of $\log(\text{EQE})$ in **Figure 5b**, where we cannot identify a constant value. Instead, the $\log(\text{EQE})$ value decreases continuously between 2.25 and 2.6 eV (grey region), where the peak at 2.25 eV is most likely due to the overlap of the onset feature with the deep tails, which show a rather constant slope (6.7 eV^{-1}), thus exponential behavior, between 1.85 and 2.05 eV (blue region, characteristic energy 150 meV). Although we acknowledge that this tail does not describe the entire EQE below 2.05 eV, we nevertheless subtract the contribution from these deep tails (dashed line in **Figure 5a**, obtained by an exponential fit between 1.85 and 2.05 eV, blue region) to disentangle it from the feature above 2.05 eV. The obtained EQE is plotted in dark green and shows a further increasing slope toward lower energy (**Figure 5b**). This leads us to conclude that an exponential fit in this spectral range might not be ideal. Therefore, we used a Gaussian fit in the range between 2.2 and 2.5 eV (red curve in **Figure 5a**; the log-slope is shown in **Figure 5b** as a red line, grey area in both graphs). The Gaussian with a maximum at 2.7 eV and a width of 0.14 eV in **Figure 5a** describes the EQE

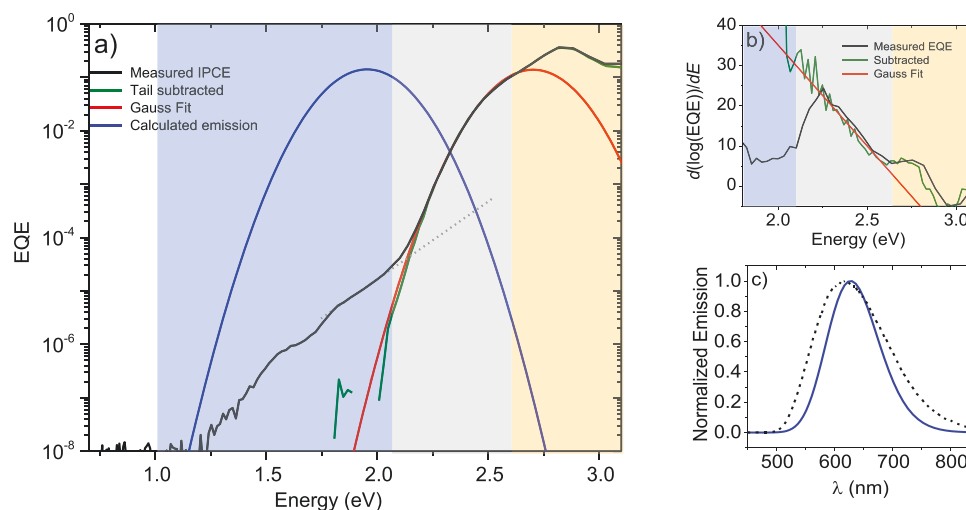


Figure 5. Reciprocity and tail states. a) Sensitive EQE of a planar device with spiro-OMeTAD as HTL (black line) and calculated emission (blue line) assuming a Gaussian feature at the absorption onset, presented with a log-scale. b) Slope of the logarithm of the EQE (black line) together with the slope of the Gaussian fit (red line) and the EQE signal after subtraction of the exponential part (dark green line). c) Calculated PL emission signal on a linear scale compared with the experimental PL (black dashed line). The colored regions in panel (a) and (b) were added as a guide for the eye.

onset well, including its shoulder at 2.6 eV. The position of the fit's maximum matches with a feature reported in PL excitation spectra in ref. [44]. Here, we use the Gaussian feature to describe the whole EQE, including the part of the spectrum that is commonly assigned to the indirect bandgap,^[14,19,46] whose reported values vary by at least 0.3 eV. We note that using a Gaussian is common for thermally broadened transitions, for example, in organic semiconductors.^[60] If we want to describe the transition from a Gaussian defect into a continuity of states (such as a broad band), we might prefer to employ an error or a logistic function.^[61] Such a fit is shown in Figure S8, Supporting Information, yielding a comparable result between 2.0 and 2.5 eV. A distribution of bandgaps could be explained by a distribution in the order of the Ag Bi occupancy,^[62] introduced during film formation and therefore influenced by the film "quality".

Having identified the Gaussian feature, we can calculate the emission spectrum scaled by the internal quantum efficiency $\phi_{Em}(E)$ using reciprocity and detailed balance ($\phi_{BB}(E)$ is the black body radiation at ambient temperature, Equation (1)).^[58]

$$\phi_{Em}(E) = EQE(E) \phi_{BB}(E) \quad (1)$$

The resulting emission spectrum is plotted in blue. Due to the broad absorption onset, a large Stokes shift is observed, similar to the behavior of organic solar cells.^[60,63] Figure 5c shows this calculated emission on a linear scale as a function of wavelength with a maximum at 630 nm. Interestingly, this spectrum looks similar to the experimental PL (dashed), although the quantitative fit is not as good as for lead-based perovskites.^[59] Nevertheless, it is strong evidence that the broad and shifted PL results from the same process as the absorption, namely a broad (indirect) bandgap distribution. Hence, more complex explanations might not be required. Also, a distinction of the absorption feature and a red luminescent state^[44] would possibly not be required.

Reasons for the discrepancy between measured and calculated emission can be found in the sample-to-sample

variations, also seen in PL measurements with peaks ranging from 500 (accompanied by distinct narrow absorption features)^[24] to 640 nm^[29] and showing narrow,^[26] distinctive,^[29] and broad^[22,27,28] shape of nominally the same material that can even be further broadened by pressure alongside with the absorption.^[43] These variations are strong indications that the states responsible for the absorption onset and emission are broad/distributed. Another point is that some of the deeper tail states seen in the IPCE, which might result from surfaces,^[64] could contribute to the asymmetric emission between 700 and 850 nm seen in the experiment (Figure 1c). Furthermore, the IQE depends on the wavelength (see above), which complicates the application of the reciprocity relation.

Nevertheless, based on this analysis we attempt to calculate the radiative V_{OC} limit by Equation (2):

$$V_{OC,rad} = \frac{k_B T}{e} \ln \left(\frac{J_{SC}}{e \int \phi_{Em}(E) dE} + 1 \right) = 1.94 \text{ V} \quad (2)$$

(with k_B : Boltzmann constant, T temperature, e elementary charge).

Here, we used $J_{SC} = 1.26 \text{ mA cm}^{-2}$ derived from the EQE.

A measured V_{OC} much lower than this value implies high non-radiative recombination losses, which can be quantified by an external luminescence yield γ , Equation (3):

$$V_{OC} = V_{OC,rad} - \underbrace{\frac{k_B T}{e} \ln \left(\frac{1}{\gamma} \right)}_{\Delta V_{OC, non-rad.}} \quad (3)$$

For a V_{OC} of 1.1 V, γ would be 10^{-14} , which is much lower than what is reported from measurements of PL yields (0.02% in ref. [37]) of films. This discrepancy indicates high recombination at the contacts, as already discussed above. To determine γ in the solar-cell device, an EL measurement was applied,

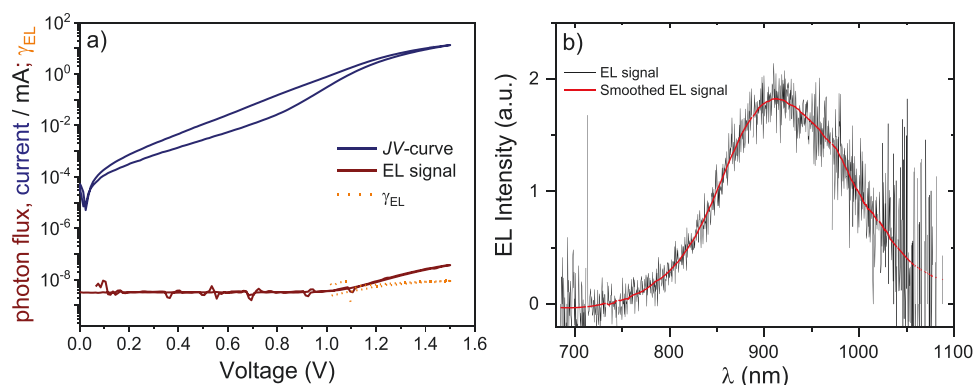


Figure 6. Electroluminescence. a) Current, emitted photon flux (multiplied by elementary charge), and the external EL quantum yield γ_{EL} , measured by a J/V loop starting at 0 V with a sweep rate of 10 mV s^{-1} . b) EL spectrum.

where the emission of the diode is measured under applied forward bias in the dark. As shown in **Figure 6a**, we succeeded in detecting emission for voltages $> 1.1 \text{ V}$ and determine an γ_{EL} of 10^{-8} . This value is orders of magnitude higher than expected from the measured V_{OC} . Taking this γ_{EL} and the measured V_{OC} , one would calculate a $V_{OC,rad}$ that is below 1.6 V. This lower $V_{OC,rad}$ could be due to the broad tail states, which we had to ignore in our analysis to make the calculations converge. Such an approach might be justified by assuming that these are non-equilibrium deep traps.^[65] A $V_{OC,rad}$ of 1.6 eV would match the $V_{OC,rad}$ of a solar cell made of our HTL P3HT,^[66] which is expected for the charge transfer and recombination in the P3HT discussed above.

Whereas **Figure 6a** shows γ_{EL} , **Figure 6b** displays the EL spectrum. In contrast to what is observed in lead-based perovskites, the EL spectrum does not coincide with the PL spectrum. Instead, the EL is strongly redshifted, showing a peak at $\approx 900 \text{ nm}$. We can only speculate on the origin of this signal. As none of the other materials in the device are expected to emit in this range (including P3HT^[67]), it is most likely that the EL results from occupation of deep tail states and the obtained γ cannot directly be used in Equation (3). Such deep tails are also seen in the EQE (blue region in **Figure 5a**), which we did not further quantify due to their complex signature, possibly modulated by interference effects.

4. Conclusion

In this work, we successfully fabricated $\text{Cs}_2\text{AgBiBr}_6$ perovskite solar cells with different architectures where we investigated different HTMs and ETLs as well as different fabrication methods in order to find answers to the question of the bottleneck that limits $\text{Cs}_2\text{AgBiBr}_6$ solar cells to 2.8% PCE so far. We analyzed the current-limiting processes by deriving the IQE from measured EQE. We find that the IQE depends on the location where photons are absorbed. Furthermore, it changes sign around V_{OC} , which is indicative of the importance of a built-in potential and non-selective contacts. Using scan-rate dependent J/V measurements, we indeed observe that charge collection strongly depends on the electric field in the device, which is affected by a slow process such as ion migration. This

is consistent with transient V_{OC} measurements that provide further evidence for high recombination rates at the contacts. Therefore, we expect that understanding the exact interplay of these processes and reducing surface recombination will allow for higher photocurrents and voltages.

We analyzed emission and absorption spectra and could describe the photocurrent onset best with a Gaussian function peaking at 2.6 eV, which might be due to disorder in the $\text{Cs}_2\text{AgBiBr}_6$ perovskite. The corresponding broad emission feature was predicted at 2.0 eV (630 nm), roughly matching measured PL.

Finally, we succeeded in measuring the EL spectrum and yield of the solar cells. The EL spectrum, found in the NIR, is strongly redshifted compared to the PL, and the EL yield is of the order of 10^{-8} . Both EL spectrum and EL yield call for further studies to unravel their origin. Overall, our work opens up pathways that can address the performance-limiting factors of $\text{Cs}_2\text{AgBiBr}_6$ and related solar cells by using the right electrode material as well as suitable charge transport materials.

Supporting Information

Supporting Information is available from the Wiley Online Library or from the author.

Acknowledgements

This work was funded by the German Federal Ministry of Education and Research (BMBF) under the agreement number 03SF0516B, the German Science Foundation (DFG) focus program SPP2196, the DFG project 382633022, the Bavarian Network "Solar Technologies Go Hybrid" (SolTech), and the DFG Excellence Cluster e-conversion (EXC 2089/1–390776260). This project has received funding from the European Union's Horizon 2020 research and innovation programme under grant agreement no. 851676 (ERC StGrt) and 795079 (Marie Skłodowska-Curie).

Conflict of Interest

The authors declare no conflict of interest.

Data Availability Statement

The data that supports the findings of this study are available in the supplementary material of this article.

Keywords

double perovskites, electroluminescence, internal quantum efficiency, lead-free perovskites, perovskite solar cells

Received: January 29, 2021

Revised: May 25, 2021

Published online:

- [1] J.-P. Correa-Baena, M. Saliba, T. Buonassisi, M. Grätzel, A. Abate, W. Tress, A. Hagfeldt, *Science* **2017**, *358*, 739.
- [2] S. Yakunin, M. Sytnyk, D. Kriegner, S. Shrestha, M. Richter, G. J. Matt, H. Azimi, C. J. Brabec, J. Stangl, M. V. Kovalenko, W. Heiss, *Nat. Photonics* **2015**, *9*, 444.
- [3] M. F. Aygüler, B. M. D. Puscher, Y. Tong, T. Bein, A. S. Urban, R. D. Costa, P. Docampo, *J. Phys. D: Appl. Phys.* **2018**, *51*, 334001.
- [4] Z.-K. Tan, R. S. Moghaddam, M. L. Lai, P. Docampo, R. Higler, F. Deschler, M. Price, A. Sadhanala, L. M. Pazos, D. Credgington, F. Hanusch, T. Bein, H. J. Snaith, R. H. Friend, *Nat. Nanotechnol.* **2014**, *9*, 687.
- [5] M. Jeong, I. W. Choi, E. M. Go, Y. Cho, M. Kim, B. Lee, S. Jeong, Y. Jo, H. W. Choi, J. Lee, J.-H. Bae, S. K. Kwak, D. S. Kim, C. Yang, *Science* **2020**, *369*, 1615.
- [6] H. Min, M. Kim, S.-U. Lee, H. Kim, G. Kim, K. Choi, J. H. Lee, S. I. Seok, *Science* **2019**, *366*, 749.
- [7] H. Lu, Y. Liu, P. Ahlawat, A. Mishra, W. R. Tress, F. T. Eickemeyer, Y. Yang, F. Fu, Z. Wang, C. E. Avalos, B. I. Carlsen, A. Agarwalla, X. Zhang, X. Li, Y. Zhan, S. M. Zakeeruddin, L. Emsley, U. Uhlir, L. Zheng, A. Hagfeldt, M. Grätzel, *Science* **2020**, *369*, 370.
- [8] A. Babayigit, A. Ethirajan, M. Muller, B. Conings, *Nat. Mater.* **2016**, *15*, 247.
- [9] Y. Hu, M. F. Aygüler, M. L. Petrus, T. Bein, P. Docampo, *ACS Energy Lett.* **2017**, *2*, 2212.
- [10] M. L. Petrus, K. Schutt, M. T. Sirtl, E. M. Hutter, A. C. Closs, J. M. Ball, J. C. Bijleveld, A. Petrozza, T. Bein, T. J. Dingemans, T. J. Savenije, H. Snaith, P. Docampo, *Adv. Energy Mater.* **2018**, *8*, 1801605.
- [11] M. L. Petrus, J. Schlipf, C. Li, T. P. Gujar, N. Giesbrecht, P. Müller-Buschbaum, M. Thelakkat, T. Bein, S. Hüttner, P. Docampo, *Adv. Energy Mater.* **2017**, *7*, 1700264.
- [12] R. Cheacharoen, C. C. Boyd, G. F. Burkhard, T. Leijtens, J. A. Raiford, K. A. Bush, S. F. Bent, M. D. McGehee, *Sustainable Energy Fuels* **2018**, *2*, 2398.
- [13] N. Glück, T. Bein, *Energy Environ. Sci.* **2020**, *13*, 4691.
- [14] E. T. McClure, M. R. Ball, W. Windl, P. M. Woodward, *Chem. Mater.* **2016**, *28*, 1348.
- [15] L.-Y. Bi, Y.-Q. Hu, M.-Q. Li, T.-L. Hu, H.-L. Zhang, X.-T. Yin, W.-X. Que, M. S. Lassoued, Y.-Z. Zheng, *J. Mater. Chem. A* **2019**, *7*, 19662.
- [16] M. K. Jana, S. M. Janke, D. J. Dirkes, S. Dovletgeldi, C. Liu, X. Qin, K. Gundogdu, W. You, V. Blum, D. B. Mitzi, *J. Am. Chem. Soc.* **2019**, *141*, 7955.
- [17] H. C. Sansom, G. Longo, A. D. Wright, L. R. V. Buizza, S. Mahesh, B. Wenger, M. Zanella, M. Abdi-Jalebi, M. J. Pitcher, M. S. Dyer, T. D. Manning, R. H. Friend, L. M. Herz, H. J. Snaith, J. B. Claridge, M. J. Rosseinsky, *J. Am. Chem. Soc.* **2021**, *143*, 3983.
- [18] S. Rieger, B. J. Bohn, M. Döblinger, A. F. Richter, Y. Tong, K. Wang, P. Müller-Buschbaum, L. Polavarapu, L. Leppert, J. K. Stolarczyk, J. Feldmann, *Phys. Rev. B* **2019**, *100*, 201404.
- [19] A. H. Slavney, T. Hu, A. M. Lindenberg, H. I. Karunadasa, *J. Am. Chem. Soc.* **2016**, *138*, 2138.
- [20] M. T. Sirtl, M. Armer, L. K. Reb, R. Hooijer, P. Dörfinger, M. A. Scheel, K. Tvingstedt, P. Rieder, N. Glück, P. Pandit, S. V. Roth, P. Müller-Buschbaum, V. Dyakonov, T. Bein, *ACS Appl. Energy Mater.* **2020**, *3*, 11597.
- [21] W. Xiang, W. Tress, *Adv. Mater.* **2019**, *31*, 1902851.
- [22] E. Greul, M. L. Petrus, A. Binek, P. Docampo, T. Bein, *J. Mater. Chem. A* **2017**, *5*, 19972.
- [23] X. Yang, Y. Chen, P. Liu, H. Xiang, W. Wang, R. Ran, W. Zhou, Z. Shao, *Adv. Funct. Mater.* **2020**, *30*, 2001557.
- [24] M. Ghasemi, L. Zhang, J.-H. Yun, M. Hao, D. He, P. Chen, Y. Bai, T. Lin, M. Xiao, A. Du, M. Lyu, L. Wang, *Adv. Funct. Mater.* **2020**, *30*, 2002342.
- [25] W. Gao, C. Ran, J. Xi, B. Jiao, W. Zhang, M. Wu, X. Hou, Z. Wu, *ChemPhysChem* **2018**, *19*, 1696.
- [26] F. Igbari, R. Wang, Z.-K. Wang, X.-J. Ma, Q. Wang, K.-L. Wang, Y. Zhang, L.-S. Liao, Y. Yang, *Nano Lett.* **2019**, *19*, 2066.
- [27] C. Wu, Q. Zhang, Y. Liu, W. Luo, X. Guo, Z. Huang, H. Ting, W. Sun, X. Zhong, S. Wei, S. Wang, Z. Chen, L. Xiao, *Adv. Sci.* **2018**, *5*, 1700759.
- [28] M. Wang, P. Zeng, S. Bai, J. Gu, F. Li, Z. Yang, M. Liu, *Sol. RRL* **2018**, *2*, 1800217.
- [29] P. Fan, H.-X. Peng, Z.-H. Zheng, Z.-H. Chen, S.-J. Tan, X.-Y. Chen, Y.-D. Luo, Z.-H. Su, J.-T. Luo, G.-X. Liang, *Nanomaterials* **2019**, *9*, 1760.
- [30] B. Wang, L. Yang, C. Dall'Agnese, A. K. Jena, S. Sasaki, T. Miyasaka, H. Tamiaki, X.-F. Wang, *Sol. RRL* **2020**, *4*, 2000166.
- [31] E. M. Hutter, M. C. Gélvez-Rueda, D. Bartesaghi, F. C. Grozema, T. J. Savenije, *ACS Omega* **2018**, *3*, 11655.
- [32] N. Pai, J. Lu, M. Wang, A. S. R. Chesman, A. Seeber, P. V. Cherepanov, D. C. Senevirathna, T. R. Gengenbach, N. V. Medhekar, P. C. Andrews, U. Bach, A. N. Simonov, *J. Mater. Chem. A* **2020**, *8*, 2008.
- [33] K. Du, W. Meng, X. Wang, Y. Yan, D. B. Mitzi, *Angew. Chem., Int. Ed.* **2017**, *56*, 8158.
- [34] Z. Li, S. R. Kavanagh, M. Napari, R. G. Palgrave, M. Abdi-Jalebi, Z. Andaji-Garmaroudi, D. W. Davies, M. Laitinen, J. Julin, M. A. Isaacs, R. H. Friend, D. O. Scanlon, A. Walsh, R. L. Z. Hoye, *J. Mater. Chem. A* **2020**, *8*, 21780.
- [35] F. Ji, J. Klarbring, F. Wang, W. Ning, L. Wang, C. Yin, J. S. M. Figueroa, C. K. Christensen, M. Etter, T. Ederth, L. Sun, S. I. Simak, I. A. Abrikosov, F. Gao, *Angew. Chem., Int. Ed.* **2020**, *59*, 15191.
- [36] R. Kentsch, M. Scholz, J. Horn, D. Schlettwein, K. Oum, T. Lenzer, *J. Phys. Chem. C* **2018**, *122*, 25940.
- [37] G. Longo, S. Mahesh, L. R. V. Buizza, A. D. Wright, A. J. Ramadan, M. Abdi-Jalebi, P. K. Nayak, L. M. Herz, H. J. Snaith, *ACS Energy Lett.* **2020**, *5*, 2200.
- [38] J. Xiu, Y. Shao, L. Chen, Y. Feng, J. Dai, X. Zhang, Y. Lin, Y. Zhu, Z. Wu, Y. Zheng, H. Pan, C. Liu, X. Shi, X. Cheng, Z. He, *Mater. Today Energy* **2019**, *12*, 186.
- [39] G. Yan, B. Jiang, Y. Yuan, M. Kuang, X. Liu, Z. Zeng, C. Zhao, J.-H. He, W. Mai, *ACS Appl. Mater. Interfaces* **2020**, *12*, 6064.
- [40] M. Pantaler, K. T. Cho, V. I. E. Queloz, I. García Benito, C. Fettkenhauer, I. Anusca, M. K. Nazeeruddin, D. C. Lupascu, C. Grancini, *ACS Energy Lett.* **2018**, *3*, 1781.
- [41] G. W. Ahn, J. H. Jo, J. Chan Kim, H. Ullah, S. Ryu, Y. Hwang, J. San Choi, J. Lee, S. Lee, H. Jeon, Y.-H. Shin, H. Y. Jeong, I. W. Kim, T. H. Kim, *J. Materiomics* **2020**, *6*, 651.
- [42] M. Keshavarz, E. Debroye, M. Ottesen, C. Martin, H. Zhang, E. Fron, R. Küchler, J. A. Steele, M. Bremholm, J. V. de Vondel,

- H. I. Wang, M. Bonn, M. B. J. Roeffaers, S. Wiedmann, J. Hofkens, *Adv. Mater.* **2020**, 32, 2001878.
- [43] C. Lv, X. Yang, Z. Shi, L. Wang, L. Sui, Q. Li, J. Qin, K. Liu, Z. Zhang, X. Li, Q. Lou, D. Yang, J. Zang, R. Liu, B. Liu, C.-X. Shan, *J. Phys. Chem. C* **2020**, 124, 1732.
- [44] A. Schmitz, L. L. Schaberg, S. Sirotinskaya, M. Pantaler, D. C. Lupascu, N. Benson, G. Bacher, *ACS Energy Lett.* **2020**, 5, 559.
- [45] L. Schade, A. D. Wright, R. D. Johnson, M. Dollmann, B. Wenger, P. K. Nayak, D. Prabhakaran, L. M. Herz, R. Nicholas, H. J. Snaith, P. G. Radaelli, *ACS Energy Lett.* **2019**, 4, 299.
- [46] M. R. Filip, S. Hillman, A. A. Haghighirad, H. J. Snaith, F. Giustino, *J. Phys. Chem. Lett.* **2016**, 7, 2579.
- [47] Y. Bekenstein, J. C. Dahl, J. Huang, W. T. Osowiecki, J. K. Swabeck, E. M. Chan, P. Yang, A. P. Alivisatos, *Nano Lett.* **2018**, 18, 3502.
- [48] W. Tress, *J. Phys. Chem. Lett.* **2017**, 8, 3106.
- [49] R. S. Sanchez, V. Gonzalez-Pedro, J.-W. Lee, N.-G. Park, Y. S. Kang, I. Mora-Sero, J. Bisquert, *J. Phys. Chem. Lett.* **2014**, 5, 2357.
- [50] E. L. Unger, A. Czudek, H.-S. Kim, W. Tress, in *Characterization Techniques for Perovskite Solar Cell Materials* (Eds.: M. Pazoki, A. Hagfeldt, T. Edvinsson), Elsevier, Amsterdam **2020**, pp. 81–108.
- [51] R. B. Dunbar, B. C. Duck, T. Moriarty, K. F. Anderson, N. W. Duffy, C. J. Fell, J. Kim, A. Ho-Baillie, D. Vak, T. Duong, Y. Wu, K. Weber, A. Pascoe, Y.-B. Cheng, Q. Lin, P. L. Burn, R. Bhattacharjee, H. Wang, G. J. Wilson, *J. Mater. Chem. A* **2017**, 5, 22542.
- [52] W. Tress, N. Marinova, T. Moehl, S. M. Zakeeruddin, M. K. Nazeeruddin, M. Grätzel, *Energy Environ. Sci.* **2015**, 8, 995.
- [53] G. Richardson, S. E. J. O’Kane, R. G. Niemann, T. A. Peltola, J. M. Foster, P. J. Cameron, A. B. Walker, *Energy Environ. Sci.* **2016**, 9, 1476.
- [54] T. Trupke, P. Würfel, I. Uhlendorf, *J. Phys. Chem. B* **2000**, 104, 11484.
- [55] W. Tress, *Organic Solar Cells*, Springer Series in Materials Science, Vol. 208, Springer International Publishing, Cham **2014**.
- [56] W. Ning, F. Wang, B. Wu, J. Lu, Z. Yan, X. Liu, Y. Tao, J.-M. Liu, W. Huang, M. Fahlman, L. Hultman, T. C. Sum, F. Gao, *Adv. Mater.* **2018**, 30, 1706246.
- [57] J. P. C. Baena, L. Steier, W. Tress, M. Saliba, S. Neutzner, T. Matsui, F. Giordano, T. J. Jacobsson, A. R. S. Kandada, S. M. Zakeeruddin, A. Petrozza, A. Abate, M. K. Nazeeruddin, M. Grätzel, A. Hagfeldt, *Energy Environ. Sci.* **2015**, 8, 2928.
- [58] U. Rau, *Phys. Rev. B* **2007**, 76, 085303.
- [59] W. Tress, N. Marinova, O. Inganäs, Mohammad. K. Nazeeruddin, S. M. Zakeeruddin, M. Graetzel, *Adv. Energy Mater.* **2015**, 5, 1400812.
- [60] K. Vandewal, K. Tvingstedt, A. Gadisa, O. Inganäs, J. V. Manca, *Nat. Mater.* **2009**, 8, 904.
- [61] C. M. Sutter-Fella, D. W. Miller, Q. P. Ngo, E. T. Roe, F. M. Toma, I. D. Sharp, M. C. Lonergan, A. Javey, *ACS Energy Lett.* **2017**, 2, 709.
- [62] J. Yang, P. Zhang, S.-H. Wei, *J. Phys. Chem. Lett.* **2018**, 9, 31.
- [63] W. Tress, B. Beyer, N. Ashari Astani, F. Gao, S. Meloni, U. Rothlisberger, *J. Phys. Chem. Lett.* **2016**, 7, 3936.
- [64] D. Bartesaghi, A. H. Slavney, M. C. Gélvez-Rueda, B. A. Connor, F. C. Grozema, H. I. Karunadasa, T. J. Savenije, *J. Phys. Chem. C* **2018**, 122, 4809.
- [65] N. Zarrabi, O. J. Sandberg, S. Zeiske, W. Li, D. B. Riley, P. Meredith, A. Armin, *Nat. Commun.* **2020**, 11, 5567.
- [66] J. Yao, T. Kirchartz, M. S. Vezie, M. A. Faist, W. Gong, Z. He, H. Wu, J. Troughton, T. Watson, D. Bryant, J. Nelson, *Phys. Rev. Appl.* **2015**, 4, 014020.
- [67] K. Tvingstedt, K. Vandewal, A. Gadisa, F. Zhang, J. Manca, O. Inganäs, *J. Am. Chem. Soc.* **2009**, 131, 11819.